

# Resonating valence bond trial wavefunctions with both static and dynamically determined Marshall sign structure

Xiaoming Zhang<sup>1,2</sup> and K. S. D. Beach<sup>1,\*</sup>

<sup>1</sup>*Department of Physics, University of Alberta, Edmonton, Alberta, Canada T6G 2E1*

<sup>2</sup>*Department of Physics and Astronomy, University of Western Ontario, London, Ontario, Canada N6A 3K7*  
(Dated: September 24, 2012)

We construct energy-optimized resonating valence bond wavefunctions as a means to sketch out the zero-temperature phase diagram of the square-lattice quantum Heisenberg model with competing nearest- ( $J_1$ ) and next-nearest-neighbour ( $J_2$ ) interactions. Our emphasis is not on achieving an accurate representation of the magnetically disordered intermediate phase (centred on a relative coupling  $g = J_2/J_1 \sim 1/2$  and whose exact nature is still controversial) but on exploring whether and how the Marshall sign structure breaks down in the vicinity of the phase boundaries. Numerical evaluation of two- and four-spin correlation functions is carried out stochastically using a worm algorithm that has been modified to operate in either of two modes: one in which the sublattice labelling is fixed beforehand and another in which the worm manipulates the current labelling so as to sample various sign conventions. Our results suggest that the disordered phase evolves continuously out of the  $(\pi, \pi)$  Néel phase and largely inherits its Marshall sign structure; on the other hand, the transition from the magnetically ordered  $(\pi, 0)$  phase is strongly first order and involves an abrupt change in the sign structure and spatial symmetry as the results of a level crossing.

## I. INTRODUCTION

Simple spin models have contributed significantly to our understanding of quantum magnetism. They consist of mutually interacting spin- $S$  objects arranged in a lattice and are meant to describe the behavior of localized electrons in a crystalline environment. Such models are generally viewed as effective, low-energy descriptions, descended from their electronic parent models by a process of integrating out the gapped charge degrees of freedom.<sup>1</sup>

A tremendous variety of spin interactions can arise. In particular, a “ $t/U$ ”-style powerseries from the strong correlation limit generates (or at least motivates) an increasingly complicated zoo of multi-spin interaction terms.<sup>2–6</sup> Nonetheless, we know that even the leading order term in the expansion, corresponding to Heisenberg models with just two-spin interactions, can display highly non-trivial physics if the exchange interactions are sufficiently frustrating.<sup>7,8</sup> In that case, the ground state may be a magnetically disordered, spin-rotation-invariant state—either liquid<sup>9</sup> or solid<sup>10,11</sup>—having no classical analogue.

Otherwise, conventional magnetic order (at some ordering vector  $\mathbf{Q}$ ) is a generic feature of the ground state for Heisenberg models in spatial dimension greater than one.<sup>12,13</sup> The absence of frustration is connected to three inter-related properties: (i) the existence of a bipartite labelling such that all antiferromagnetic interactions connect sites in opposite sublattices, (ii) strict adherence to a Marshall sign rule,<sup>14</sup> and (iii) the possibility of transforming mechanistically to a basis in which all amplitudes of the wavefunction are real and nonnegative. The last of these is why nonfrustrated models can be easily simulated using quantum Monte Carlo approaches.<sup>15–17</sup>

For the  $S = 1/2$  case, all three properties are conceptually unified in the language of *valence bonds*.<sup>18–22</sup> The collinear,  $\mathbf{Q}$ -ordered ground state of a nonfrustrated

Heisenberg model can be described in a bipartite valence bond basis<sup>22,23</sup> in which the AB sublattice labelling coincides with the alternating pattern laid out by  $\mathbf{Q}$  and only spins in opposite sublattices are bound into singlet pairs. In terms of such a basis  $\mathcal{V}_{AB} = \{|v\rangle\}$ , the ground state has an expansion  $|\psi\rangle = \sum_v \psi(v)|v\rangle$  in which each amplitude  $\psi(v)$  is real and nonnegative. The exact amplitudes can be obtained numerically by projection.<sup>24–27</sup>

It is also possible to find extremely good approximate values of the form  $\psi(v) \approx \prod_{[i,j] \in v} h(\mathbf{r}_{ij})$ , where  $h(\mathbf{r}) > 0$  is a function of the vector connecting bond end points. This resonating valence bond (RVB) ansatz, due to Liang, Doucot, and Anderson,<sup>28</sup> strictly enforces the geometric tiling constraint on the singlet bonds but ignores additional bond-bond correlations.<sup>29</sup> For a magnetically ordered state, one can show that factorizability into individual bond amplitudes is the correct assumption.<sup>30,31</sup> Moreover, for nonfrustrated systems, the amplitudes exhibit powerlaw decay, and hence the wavefunction contains bonds on all length scales.

As a specific and illustrative example, we consider the square-lattice  $J_1$ – $J_2$  model for spin half. It has two nonfrustrated limits. The model with antiferromagnetic nearest-neighbour interactions only ( $J_1 = 1, J_2 = 0$ ) exhibits a Néel ordered ground state whose staggered moment is roughly 60% of its fully polarized, classical value. The state is almost perfectly captured by an RVB wavefunction whose bond amplitudes are computed as  $h(\mathbf{r}) = \sum_{\mathbf{q}} e^{i\mathbf{q}\cdot\mathbf{r}} [1 - (1 - \gamma_{\mathbf{q}}^2)^{1/2}] / \gamma_{\mathbf{q}}$ . Here,  $\gamma_{\mathbf{q}} = (\cos q_x + \cos q_y)/2$ , and the wavevector sum is taken over a Brillouin zone reduced with respect to  $\mathbf{Q} = (\pi, \pi)$ . The opposite limit, with *next*-nearest-neighbour interactions dominating ( $J_1 = 0^+, J_2 = 1$ ), is equivalent to two interpenetrating nearest-neighbour Heisenberg antiferromagnets rotated  $45^\circ$ . The spin directions in the two otherwise disjoint subsystems lock to each other<sup>32</sup> provided

that  $J_1$  is not strictly zero. In this case, the ground state is equally well described by the RVB wavefunction, but with the substitution of  $\gamma_{\mathbf{q}} = \cos q_x \cos q_y$  and a Brillouin zone defined modulo  $\mathbf{Q} = (\pi, 0)$  or  $\mathbf{Q} = (0, \pi)$ .

What we present in this paper is an attempt to interpolate between these two limits—through the entire range of relative couplings that are highly frustrated—using the RVB state as a variational wavefunction. Our approach is inspired by Ref. 33, but there are several important differences. The first is simply the scale of the calculation: we have simulated a large number of lattice sizes up to  $L = 32$  on a dense grid of relative coupling values ( $g = J_2/J_1$  ranging from 0 to 1 in steps of 0.01). Second, we do not require that  $h(\mathbf{r})$  respect the full  $C_4$  symmetry of the square lattice. Rather, we impose only the x- and y-axis reflection symmetry, giving the amplitudes an opportunity either to acquire (over the course of the energy optimization) the full symmetry or to settle into a state that looks different under  $90^\circ$  rotation. Third, we explore the space of AB sublattice labellings by which the bipartite valence bond basis is constructed.

As in Ref. 33, we make use of an unbiased, stochastic optimization scheme. Changes to the  $h(\mathbf{r})$  values are made according to the sign of the local energy gradient. Step sizes are randomized, and their magnitude decreases on a powerlaw schedule. We do not attempt to guide the optimization, other than to ensure that none of the bond amplitudes goes negative; nor do we impose any constraints on the variational parameters based on any prior knowledge (gleaned, e.g., from mean field theory<sup>30</sup> or from a master equation analysis<sup>34</sup>).

We discover the following. At this level of approximation, the  $J_1$ – $J_2$  model does indeed support a magnetically disordered intermediate phase. But its width is much smaller than expected: the phase boundaries are found to be at  $g_{c1} \doteq 0.54(1)$  and  $g_{c2} \doteq 0.5891(3)$ . The transitions are unambiguously second- and first-order, respectively, with the ground state always achieving the full  $C_4$  symmetry for  $g < g_{c2}$ . As the system is tuned up from  $g = 0$ , increasing frustration eventually extinguishes the  $(\pi, \pi)$  ordered moment at  $g_{c1}$  in a continuous fashion.

The disappearance of magnetic order is preceded by a failure of the Marshall sign rule at  $g_{M1} \doteq 0.398(4)$ . Still, even though the rule is not strictly obeyed beyond  $g_{M1}$ , the Marshall structure inherited from the  $g = 0$  model remains largely in tact throughout the intermediate phase. This is true in the sense that continuing to define the bipartite bond basis from a *checkerboard* sublattice decomposition produces only a microscopic number of negative  $h(\mathbf{r})$  values—only  $h(\pm 1, \pm 2)$  and  $h(\pm 2, \pm 1)$  initially. Moreover, when we allow the AB pattern to arise on its own within the simulation (described in detail in Secs. II D and III), the checkerboard pattern is the one selected whenever  $g < g_{c2}$ .

On the other hand, the RVB state at large  $g$  explicitly breaks the  $90^\circ$  rotation symmetry and has a Marshall sign structure based on a *stripe* sublattice decomposition. As the coupling is tuned down from the  $g = \infty$

limit, the  $(\pi, 0)$  ordered moment is not strongly affected, and it persists with only weak variation (never dropping below 47% of its fully polarized value) down to  $g_{c2}$ , where the spatially symmetric, checkerboard-based RVB wavefunction takes over as the lowest energy state. This state in the region  $g_{c1} < g < g_{c2}$  is, as far as we can tell, featureless. It exhibits no long-range spin or dimer order, and it breaks no symmetries. It is not, however, a “short range RVB state” in the usual sense, since it is not made up of predominantly short bonds. Its amplitude function  $h(\mathbf{r})$  is highly anisotropic (as anticipated elsewhere<sup>34</sup>) and remains long ranged along the principle spatial axes. Spin correlations appear to be critical, and dimer correlations decay either exponentially or with a high power law. This is in stark contrast to the usual short-bond-only RVB state, which has spin correlations that decay exponentially<sup>28</sup> and dimer correlations that decay algebraically.<sup>35,36</sup> The presence of long bonds implies an absence of the topological order<sup>35,36</sup> that is characteristic of the purely short ranged RVB state in two dimensions.

## II. MODEL AND METHOD

### A. Frustrated Hamiltonian

The spin-half, square-lattice Heisenberg model with frustrating interactions has a Hamiltonian

$$H = J_1 \sum_{\langle i,j \rangle} \mathbf{S}_i \cdot \mathbf{S}_j + J_2 \sum_{\langle\langle i,j \rangle\rangle} \mathbf{S}_i \cdot \mathbf{S}_j, \quad (1)$$

where  $J_1 > 0$  and  $J_2 > 0$  are the antiferromagnetic exchange couplings. The summations range over pairs of adjacent sites  $\langle i, j \rangle$  and over farther pairs  $\langle\langle i, j \rangle\rangle$  that sit diagonally across a plaquette. The ratio  $g = J_2/J_1$  is the key tuning parameter at zero temperature. In the classical version of this model ( $S \rightarrow \infty$ ), two magnetic phases meet at exactly  $g = 0.5$ , separated by a first-order transition.<sup>53–56</sup>

In the  $S = 1/2$  problem, the two magnetically ordered ground states obtain for values  $g \lesssim 0.4$  and  $g \gtrsim 0.6$ ,<sup>37–42</sup> and a magnetically disordered phase intervenes. (There is, however, a good deal of disagreement over the exact positions of the critical points; cf. Refs. 45 and 68, which put the lower critical point as low as 0.35 and as high as 0.45.) The physics of the phase in the intermediate region is not known with complete certainty, but it is believed to be short ranged and not to exhibit any kind of conventional magnetic order. One possibility is a crystalline arrangement of valence bonds, a state with broken translational symmetry in which singlet formation favours an enlargement of the unit cell beyond that of the underlying square lattice.<sup>57–70</sup> A featureless spin liquid that doesn’t break any symmetries was also proposed as a possible ground state.<sup>49,71–80</sup>

The case for a spin liquid has been advanced by recent tensor product<sup>81</sup> and density matrix renormaliza-

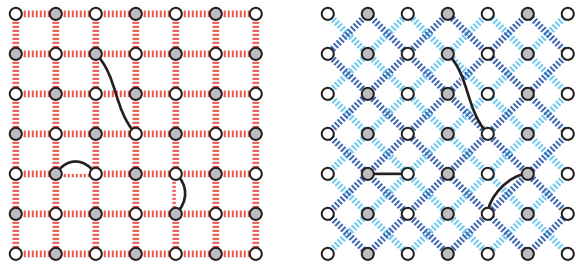


FIG. 1. (color online) Dashed lines indicate the  $J_1$  (red) and  $J_2$  (blue) exchange couplings. The basis contains only product states of singlets connecting sites in opposite sublattices. (Left) In the limit  $g = J_2/J_1 = 0$ , a checkerboard pattern of A and B labels that coincides with  $(\pi, \pi)$  magnetic order. (Right) In the limit  $g = \infty$ , a stripe pattern that coincides with  $(\pi, 0)$  order. In each case, three permissible singlet pairings are indicated.

tion group calculations.<sup>82</sup> With regard to the latter result, Sandvik has suggested that the use of a cylindrical geometry complicates the detection of crystalline order.<sup>83</sup> His numerical experiments seem to indicate that the mixture of open and closed boundary conditions significantly raises the crossover length scale  $\xi$  beyond which bond order takes hold (i.e., where the finite size scaling behaviour of the dimer-dimer correlations is truly in the asymptotic regime). Such questions are difficult to resolve. Unlike in three-dimensional systems, where crystalline bond order, if it is present, is almost always strong,<sup>5,89</sup> in two dimensions it is quite delicate and can easily be disguised by a  $U(1)$  effective symmetry for system sizes  $L \lesssim \xi$ . (See Sects. III and IV of Ref. 90 and references therein.) Here, we attempt to make the best of this unsatisfactory state of affairs. We simply take the point of view that, for the lattice sizes (up to  $L = 32$ ) we can simulate, the liquid and the weakly ordered bond crystal are indistinguishable.

## B. RVB trial wavefunction

In quantum Heisenberg models, competing interactions that frustrate the order have the potential to stabilize exotic quantum phases, but they also render the problem computationally intractable on large lattices. Frustrating interactions of even infinitesimal strength cause a sign problem<sup>43</sup> that makes quantum Monte Carlo calculations unfeasible. Moreover, the size of the Hilbert space grows exponentially with system size and is thus beyond the capability of exact diagonalization (ED) calculations if we want to get near the thermodynamic limit. (The record for spin half has recently jumped from 42 sites<sup>44–46</sup> to 48 sites,<sup>47</sup> a terribly impressive technical feat that nonetheless limits us to two-dimensional length scales  $\sim \sqrt{48}$  that are quite small.) An approximate

method based on good trial wavefunctions is therefore one of the few remaining possibilities for large systems.

We consider a lattice of  $2N$  spins and a factorizable RVB wavefunction of the form

$$|\psi\rangle = \sum_v \prod_{[i,j] \in v} h_{ij} |v\rangle, \quad (2)$$

where the sum is over all partitions of the lattice into  $N$  directed pairs  $v = ([i_1, j_1], [i_2, j_2], \dots, [i_N, j_N])$ . To every such *dimer covering*  $v$ , there is a corresponding singlet product state; e.g.,

$$|v\rangle = \frac{1}{2^{N/2}} \bigotimes_{[i,j] \in v} \left( |\uparrow_i \downarrow_j\rangle - |\downarrow_i \uparrow_j\rangle \right) \quad (3)$$

in the  $S = 1/2$  case. The set  $\mathcal{V} = \{|v\rangle\}$  of all possible singlet product states is both overcomplete and nonorthogonal and constitutes the so-called *valence bond basis*.

We can now break up the lattice into two sublattices—groups of sites labelled A and B, equal in number—and restrict ourselves to a reduced basis in which valence bonds only connect sites in opposite sublattices (i.e.,  $v \in \mathcal{V}_{AB} \simeq S_N$ , rather than  $v \in \mathcal{V} \simeq S_{2N}/Z_2^N$ ). We adopt the convention that each bond  $[i, j]$  is arranged with site  $i$  in sublattice A and site  $j$  in sublattice B. This has the advantage of rendering the overlap strictly positive:  $\langle v | v' \rangle = 2^{N_l(C) - N}$ , where  $N_l(C)$  is the number of loops in the double dimer covering  $C = (v, v')$ . (In this “bosonic” convention, the singlets are AB directed bonds. In the complementary “fermionic” convention, the bonds are directionless and all signs are moved into the overlaps.<sup>48–52</sup>)

To start, we consider two families of trial state, each built using a bipartite bond basis consistent with one of two static choices of sublattice labelling, viz., the checkerboard and stripe patterns shown in Fig. 1. Later in the paper, we go on to describe a procedure in which the trial state is built using an unrestricted bond basis and in which the sublattice labelling (and hence the Marshall sign convention) is determined dynamically.

The RVB wavefunction is quite expressive. Its degrees of freedom are the full set of  $h(\mathbf{r})$  values with the bond vector  $\mathbf{r}$  spanning all lengths and orientations that can be achieved on an  $L \times L$  cluster with periodic boundary conditions and that are unique up to whatever symmetries are enforced. (Still, the total number of parameters grows only linearly with the number of spins, which is radically slower than the number of states in the total spin singlet sector.) Previous calculations of this kind<sup>33,34</sup> considered just the checkerboard AB pattern and imposed on  $h(\mathbf{r}) = h(x, y)$  the full symmetry of the lattice, such that  $h(x, y) = h(|x|, |y|) = h(|y|, |x|)$ . In this calculation, we impose a less restrictive condition,  $h(x, y) = h(|x|, |y|)$ , that respects reflection symmetry across the lines  $x = 0$  and  $y = 0$  but not across the lines  $y = \pm x$ . For the checkerboard pattern, the number of free parameters is  $(L/2 - \eta)(L/2 - 1)$ , where  $\eta = (L/2 \bmod 2)$  distinguishes between  $L/2$  even and

odd. For the stripe pattern, the count is only slightly higher:  $(L/2 + 1)(L/2 - 1) = L^2/4 - 1$ .

To recapitulate, our work involves a basis choice. We do not construct the trial wave functions from the largest possible set of valence bond states in which the spins are joined in all possible ways. Instead, we obtain a more restricted basis by dividing the system into two groups of sites (A and B) and only keeping states in which bonds connect A sites and B sites (bipartite bonds). No approximation is involved in this basis choice since the restricted basis is so massively overcomplete that even this subset still spans the relevant part of the Hilbert space.

But in assigning A and B labels to the sites, we are making choices about the form of the trial wavefunction. By working with the checkerboard and stripe AB patterns, we are in essence adapting the trial wavefunction to  $g = 0$  and  $g = \infty$  and taking advantage of the Marshall's sign rules that exist in the two limits. However, we are not biasing the wavefunction insofar as we are building in any kind of magnetic order. The wavefunctions constructed from either AB pattern are fully capable of representing non-magnetic states.

### C. Sampling algorithm

Every measurement  $\langle \psi | \hat{O} | \psi \rangle / \langle \psi | \psi \rangle$  can be thought of as the ensemble average of an appropriate estimator  $O : C \rightarrow O(C)$  in the gas of fluctuating loops described by

$$Z = \frac{1}{q^N} \sum_C q^{N_l(C)} \prod_{[i,j] \in C} h_{ij}. \quad (4)$$

Here,  $C = (v, v')$  is a loop configuration arising from the superposition of two dimer coverings,  $N_l(C)$  counts the number of loops, and  $q = 2$  is the loop fugacity appropriate for  $S = 1/2$ . When Marshall's theorem holds, the bond amplitudes satisfy  $h_{ij} \geq 0$  and thus every term in Eq. (4) is nonnegative. This model is amenable to Monte Carlo simulation. We now outline a simple and efficient algorithm for performing the stochastic sampling.

As a formal trick (in the spirit of Ref. 84), we enlarge the phase space from  $\Phi_0$  to  $\Phi_0 \times \Phi_1 \times \dots \times \Phi_N$ , where  $\Phi_n$  is the set of configurations in which  $2n$  free endpoints have been introduced by breaking  $n$  valence bonds. (The system has been converted to one of both closed loops and open strings.) We take the partition function to be

$$Z = \frac{1}{q^N} \sum_C q^{N_l(C)} \sigma^{N_s(C)} \prod_{[i,j] \in C} h_{ij}. \quad (5)$$

The configurations  $C$  are now assembled from all possible partial coverings  $v = ([i_1, j_1], [i_2, j_2], \dots, [i_n, j_n])$  of variable length  $0 \leq n \leq N$ , and  $\sigma$  is introduced as a fugacity for the open strings (numbering  $N_s(C) = N - n$ ). The loop-only sector corresponds to the original partition function,  $Z_0 = \langle 1 \rangle_{\Phi_0}$ . (In each string sector there

is a Green's function defined by the string endpoints:  $G_{ij} = \langle \delta_{i,\alpha_1} \delta_{j,\beta_1} \rangle_{\Phi_1}$ ,  $G_{ij;kl} = \langle \delta_{i,\alpha_1} \delta_{j,\beta_1} \delta_{k,\alpha_2} \delta_{l,\beta_2} \rangle_{\Phi_2}$ , etc., and  $Z_0 = \langle 1 \rangle_{\Phi_0}$ . Here  $\alpha_n$  and  $\beta_n$  denote the positions of the head and tail of the  $n^{\text{th}}$  string. It is worth emphasizing that these  $2n$ -point Green's functions do not coincide with expectation values of the physical spin operators. In general, we must take all measurements in the  $\Phi_0$  configuration space using the loop estimators derived in Ref. 22.)

We will consider a process that involves breaking a single valence bond ( $\Phi_0 \rightarrow \Phi_1$ ) to produce an open string whose two endpoints (the "head" and "tail") serve as walkers subject to Monte Carlo updates. The walkers move via a series of two-step motions that involve drawing a new bond and erasing an old one. When the walkers meet the loop is closed ( $\Phi_1 \rightarrow \Phi_0$ ). Figure 2 shows an example circuit. The five successive steps shown in panels (b)–(f) produce an overall change in the relative weight

$$\frac{\sigma}{h_{5,4}} \times \frac{h_{1,2}}{qh_{1,4}} \times \frac{h_{5,8}}{qh_{7,8}} \times \frac{qh_{3,2}}{h_{3,6}} \times \frac{h_{7,6}}{\sigma}. \quad (6)$$

Since we have chosen the bond amplitudes  $h_{ij}$  to be nonnegative, we can define a local amplitude  $H_i = \sum_j h_{ij}$  and a total overall amplitude  $H = \sum_i H_i = \sum_{ij} h_{ij}$ . These definitions will be useful in the derivations that follow.

To begin let us consider processes that take the system from the space of loops to the space of loops and one string. We move from a configuration  $C \sim [i, j]$  to a configuration  $C' \sim (i)(j)$  by breaking a bond  $[i, j]$  and thus leaving string endpoints  $(i)$  and  $(j)$ . The transition probabilities for breaking and repairing the bond obey the detailed balance equation

$$W_{[i,j]}^{\text{break}} P(i) \pi_C = W_{(i)(j)}^{\text{repair}} P(j|i) \pi_{C'}. \quad (7)$$

Here  $P(i)$  is the probability of choosing a site  $i$  whose bond we want to break, and  $P(j|i)$  is the probability of choosing  $j$  given a walker (string endpoint) at site  $i$ .  $\pi_C$  and  $\pi_{C'}$  represent the likelihood of the system being found in configurations  $C$  and  $C'$ . Their ratio is given by

$$\frac{\pi_{C'}}{\pi_C} = \frac{\sigma}{h_{ij}}. \quad (8)$$

If we choose which bond to break according to the distribution of local bond weight  $P(i) = H_i/H$  and choose walker movements according to the distribution  $P(j|i) = h_{ij}/H_i$ , then

$$\delta = \frac{W_{[i,j]}^{\text{break}}}{W_{(i)(j)}^{\text{repair}}} = \frac{P(j|i) \pi_{C'}}{P(i) \pi_C} = \frac{\sigma}{H}. \quad (9)$$

We are free to choose  $\sigma = H$ , in which case  $W_{[i,j]}^{\text{break}} = W_{(i)(j)}^{\text{repair}} = 1$ .

For motion of the walkers within  $\Phi_1$ , we need to know the transition rates between configurations  $C \sim (i)[j, k]$

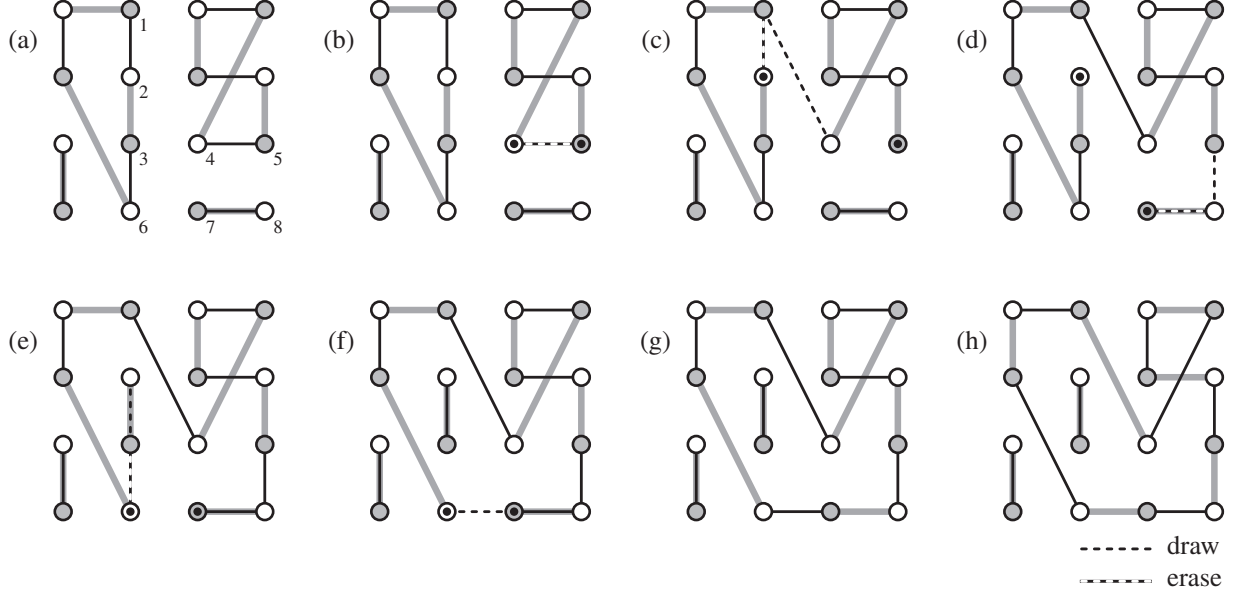


FIG. 2. (a) Two superimposed valence bond configurations form a collection of closed loops. Eight of the sites are numbered for use in Eq. (6). (b) Breaking one bond leaves an open string with a head and tail located at the former bond's endpoints. (c)–(e) The head and tail move by drawing a new bond and erasing the preexisting bond emerging from the destination site. (f) The open string is closed when the head and tail reconnect. (g) The repaired loop configuration. (h) Exchanging the background and foreground links in any loop is also a valid update.

and  $C' \sim [i, j](k)$ . This represents a process in which a walker at  $i$  draws a new bond to some site  $j$  and then erases the preexisting bond connecting  $j$  to  $k$ , thus leaving the walker at site  $k$ . The detailed balance equation is

$$W_{i \rightarrow k}^{\text{walk}} P(j|i) \pi_C = W_{k \rightarrow i}^{\text{walk}} P(j|k) \pi_{C'}. \quad (10)$$

The ratio

$$\frac{\pi_{C'}}{\pi_C} = q^{\delta N_l} \frac{h_{ij}}{h_{jk}} \quad (11)$$

depends on  $\delta N_l = N_l(C') - N_l(C) = \pm 1$  (or 0 if the moves do not respect a fixed lattice bipartition; see discussion in Sect. II D). As before, we attempt moves according to the distribution  $P(j|i) = h_{ij}/H_i$ . Then

$$\delta_{ik}^{\text{walk}} = \frac{W(i \rightarrow k)}{W(k \rightarrow i)} = \frac{P(j|k)}{P(j|i)} \frac{\pi_{C'}}{\pi_C} = \frac{H_i}{H_k} q^{\pm 1}, \quad (12)$$

which can be solved as  $W_{i \rightarrow k}^{\text{walk}} = \delta/(1 + \delta)$  or  $W_{i \rightarrow k}^{\text{walk}} = \min(1, \delta)$ .

Note that the transition rate does not depend on the ratio of bond amplitudes, as it would if we had, for example, selected a site uniformly with  $P(j|i) = 1/N$ . The ratio  $h_{ij}/h_{jk}$  may fluctuate wildly over many orders of magnitude, so subsuming it into the sampling maximizes the efficiency of the algorithm.

In the case of a translationally invariant system, the amplitude for pairing spins at  $i$  and  $j$  must be a function of the vector  $\mathbf{r}_{ij}$  connecting the two sites; i.e.,  $h_{ij} = h(\mathbf{r}_{ij})$ . Hence,  $H = H/N = H_i = \sum_{\mathbf{r}} h(\mathbf{r})$  for all  $i$ ,

which implies that  $P(i) = H_i/H \rightarrow 1/N$  is uniform and  $P(j|i) = h_{ij}/H_i \rightarrow h(\mathbf{r}_{ij})/H$ . The algorithm can be summarized as follows:

1. Pick any valence bond  $[i, j]$  (by choosing  $i$  uniformly from the set of A sublattice sites and then selecting its partner site in  $v$  or  $v'$ ) and break it. The resulting string has endpoints at  $\mathbf{R} = \mathbf{r}_i$  and  $\mathbf{R}' = \mathbf{r}_j$ .
2. To move the head, choose a new bond vector  $\mathbf{r}$  from the distribution  $h(\mathbf{r})/H$ . So long as  $\mathbf{R} + \mathbf{r} \neq \mathbf{R}'$ , attempt to draw a new bond from  $\mathbf{R}$  to  $\mathbf{R} + \mathbf{r} = \mathbf{r}_k$  (for some  $k$ ). The bond that already exists at that site  $[k, l]$  is then erased and the walker is moved to  $\mathbf{r}_l$ . The move is accepted with probability 1 if it splits two loops and with probability 1/2 if it joins two loops.
3. Otherwise, if  $\mathbf{R} + \mathbf{r} = \mathbf{R}'$ , close the open string by drawing a new valence bond from  $\mathbf{R}$  to  $\mathbf{R}'$ .

The worm algorithm described here is ergodic and guaranteed to have a high acceptance rate. This is in contrast to the original bond-swap scheme proposed in Ref. 28, wherein two A-site or B-site bond endpoints sitting diagonally across a plaquette are swapped using Metropolis sampling. This antiquated algorithm runs into difficulty when the function  $h(\mathbf{r})$  is short ranged. In particular, short bonds that are adjacent but not sharing a common plaquette generate long bonds under rearrangement, so whenever the amplitudes for long bonds

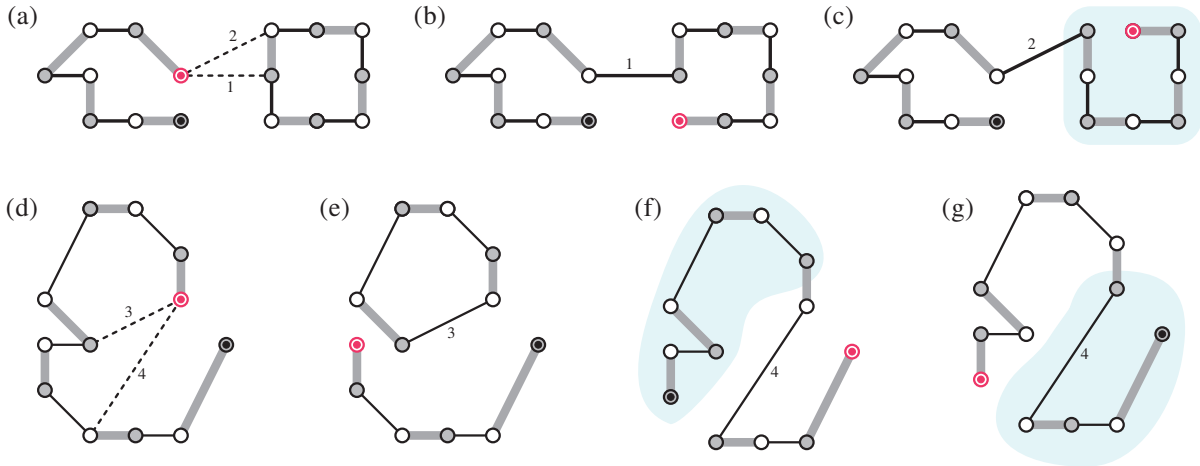


FIG. 3. (color online) (a) Two possible paths, marked 1 and 2, take the worm head to a site in the opposite or same sublattice of another closed loop. In either case, the loop is absorbed. (b) Path 1 leads to a rearrangement of the worm that preserves the AB labelling. (c) Path 2 requires that the AB labelling be reversed in the highlighted region. (d) Another worm, following two possible paths marked 3 and 4. (e) For path 3, the AB labelling is preserved, and the worm emits a new closed loop. (f,g) Path 4 requires that the AB labelling be reversed in the highlighted region. The number of loops remains unchanged.

become small, the acceptance rate can become correspondingly small. Hence, ergodicity breaks down. Worse, there are typically many trapping configurations from which the simulation cannot emerge. The worm algorithm does not suffer from these problems, because it can traverse any local barriers by stepping outside the space of closed loops. (We make no claims of novelty in this regard. Various approaches to overcome the sampling difficulty have been presented elsewhere.<sup>35,36,91</sup>)

#### D. Fluctuating sublattice assignment

The discussion in the previous section was specific to the case in which (i) the AB pattern is regular and (ii) the  $\mathbf{r}$  vectors that have nonzero  $h(\mathbf{r})$  only connect sites in opposite sublattices. If those conditions hold, there are only two possible consequences to the motion of the open string: a loop is joined to the string ( $\delta N_l = -1$ ) or a loop is split off from it ( $\delta N_l = +1$ ). In both cases, represented in Fig. 3 by panels (a)→(b) and (d)→(e), the AB pattern itself is left undisturbed.

More generally, as the open string propagates it lays down a chain of singlet bonds whose alternating site labels may be at odds with the traversed sites' current AB assignments. A simple workaround is to flip the sublattice labels as required to correct the mismatch. The relevant processes are now those in which a moving open string absorbs a closed loop ( $\delta N_l = -1$ ) or reorganizes itself without impinging on any additional sites ( $\delta N_l = 0$ ). The first case is depicted in Fig. 3 by panels (a)→(c) and the second by (d)→(f) or (d)→(g). A crucial consideration is that, since the singlets are directional, flipping sublattice labels along a loop segment has the effect of reversing a chain of singlet bonds. If an odd number of

singlets is effected, the overall sign of the wavefunction will change. This is true for all  $\delta N_l = 0$  worm steps.

The sublattice mismatch can either be a temporary condition—lasting only until the worm updates succeed in laying down a global AB pattern that is an invariant of the worm motion—or it may be that the motion described by a given  $h(\mathbf{r})$  is incompatible with any static AB site labelling. For example, consider the one-parameter family of short range states on the square lattice described by  $h(\pm 1, 0) = h(0, \pm 1) = \cos \theta$  and  $h(\pm 1, \pm 1) = \sin \theta$  (with  $0 \leq \theta \leq \pi/4$ ). Regardless of the initial sublattice labelling—it can be any random assignment having an equal number of A and B labels—the simulation will dynamically establish the checkerboard pattern provided that  $\theta = 0$ . We keep track of the AB labelling pattern by measuring a function  $\Lambda(\mathbf{Q}) = \sum_{\mathbf{r}, \mathbf{r}'} e^{i\mathbf{Q} \cdot (\mathbf{r} - \mathbf{r}')} \langle \lambda(\mathbf{r}) \lambda(\mathbf{r}') \rangle$ , where  $\lambda(\mathbf{r})$  takes the value  $-1$  or  $1$  depending on the current sublattice assignment at site  $\mathbf{r}$ . If  $\theta = 0$ ,  $\Lambda(\mathbf{Q})$  starts off broad but systematically flows toward the distribution with a single delta function peak at  $\mathbf{Q} = (\pi, \pi)$ ; once that is achieved, the pattern ceases to evolve. Similar behaviour is exhibited at  $\theta = \pi/4$ , where the system settles into a static pattern with either  $\mathbf{Q} = (\pi, 0)$  or  $\mathbf{Q} = (0, \pi)$ . Only in those two extreme cases is the sublattice pattern eventually static and the simulation sign-problem free.

### III. RESULTS

As a test of the worm implementation, we compare its output to analytical results obtained for the  $4 \times 4$  lattice. We exploit the fact that the bipartite valence bond basis  $\mathcal{V}_{AB}$  for  $2N$  spins is isomorphic to the set of permutations on  $N$  elements.<sup>22</sup> Hence, the basis states have a natural



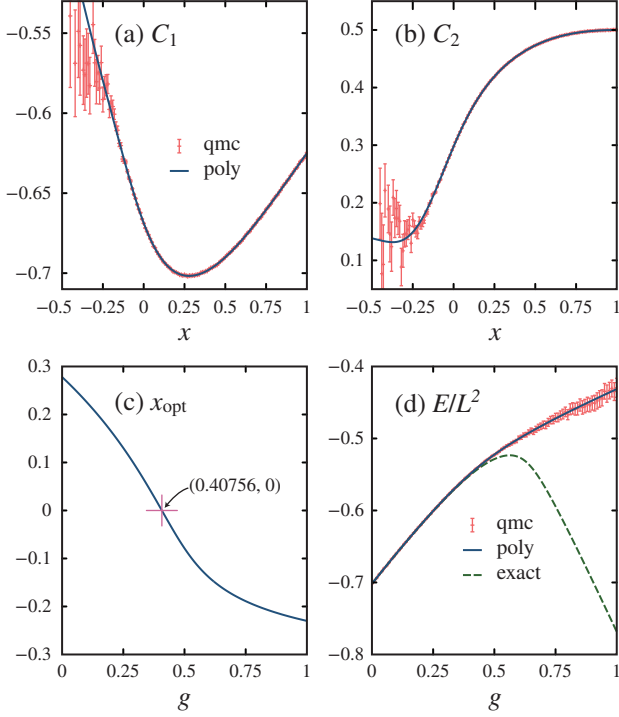


FIG. 4. (color online) (a),(b) Spin correlations  $C_1$  and  $C_2$  between nearest- and next-nearest-neighbour spins, computed for the RVB trial wavefunction as a function of the amplitude ratio  $x = h(2,1)/h(1,0)$ . As  $x$  becomes increasingly negative, numerical evaluation becomes dominated by noise from the sign problem. (c) The energy-optimized value  $x_{\text{opt}}$  remains positive up to a  $g = J_2/J_1 = 0.40756$ . (d) The optimized trial state gives a good approximation to the true ground state energy up to where the Marshall sign rule breaks down.

lexical ordering via the Lehmer code<sup>87,88</sup> and can easily be enumerated. For  $4 \times 4 = 16$  sites, the total number of the states is only  $8! = 40320$ , which means that expectation values of the trial wavefunction can be evaluated exactly at very little computational cost. Moreover, we can carry out the calculation symbolically. Each observable takes the form of a rational function of order  $[16,16]$ :

$$\langle O \rangle = \frac{O(x)}{Z(x)} = \frac{3 \sum_{k=0}^{16} o_k x^k}{4 \sum_{l=0}^{16} z_l x^l}. \quad (13)$$

The argument of the polynomials appearing in the numerator and denominator is the real-valued ratio  $x = h(2,1)/h(1,0)$ , and the coefficients are all integers. Coefficients for various observables are listed in Table I.

For this test we have focussed on the nearest- and next-nearest-neighbour spin correlation functions  $C_1 = \sum_{\langle i,j \rangle} \langle \mathbf{S}_i \cdot \mathbf{S}_j \rangle$  and  $C_2 = \sum_{\langle\langle i,j \rangle\rangle} \langle \mathbf{S}_i \cdot \mathbf{S}_j \rangle$ ; the  $\mathbf{Q} = (\pi, \pi)$  staggered and  $\mathbf{Q} = (\pi, 0)$  stripe magnetization via  $M_{\mathbf{Q}}^2 = \frac{1}{L^4} \sum_{\mathbf{r}, \mathbf{r}'} (-1)^{i\mathbf{Q} \cdot (\mathbf{r} - \mathbf{r}')} \langle \mathbf{S}_{\mathbf{r}} \cdot \mathbf{S}_{\mathbf{r}'} \rangle$ ; and  $D_x^2 = \frac{1}{L^4} \sum_{\mathbf{r}, \mathbf{r}'} (-1)^{e_x \cdot (\mathbf{r} + \mathbf{r}')} \langle (\mathbf{S}_{\mathbf{r}} \cdot \mathbf{S}_{\mathbf{r} + \mathbf{e}_x}) (\mathbf{S}_{\mathbf{r}'} \cdot \mathbf{S}_{\mathbf{r}' + \mathbf{e}_x}) \rangle$ , the order parameter for a columnar dimer crystal. We have

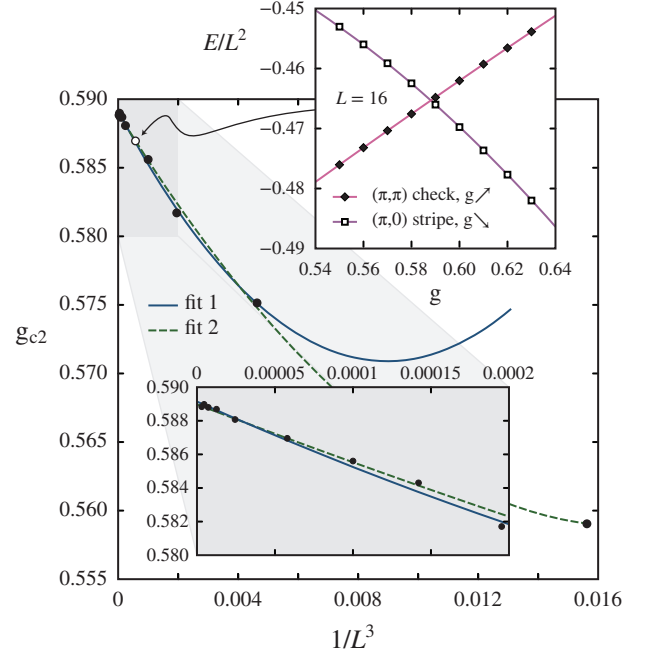


FIG. 5. (color online) The level crossings are plotted versus  $1/L^3$  and extrapolated to the thermodynamic limit. Several different second-order polynomial fits (two shown) are used to estimate the uncertainty in the intercept. The solid, blue line (fit 1) is an attempt to fit the  $L \geq 6$  data to  $c_0 \exp(c_1 x + c_2 x^2)$ ; the dashed, green line (fit 2) is a fit to  $c_0 + c_1 L^{-3} + c_2 L^{-6}$  for  $L \geq 4$ . Our analysis suggests a value  $g_{c2} \doteq 0.5891(3)$ . The upper inset shows the analysis behind the  $L = 16$  data point, which is marked in the main graph as an open circle. The lower inset is a magnification of the shaded region.

verified that the the worm algorithm, conventional bond swap Monte Carlo, and exact evaluation give consistent results for all these quantities. The comparison for the energetics is shown in Fig. 4. Note that in Figs. 4(a) and 4(b), the stochastic evaluation continues to work in some range of  $x < 0$  but quickly breaks down as  $x$  becomes strongly negative. The optimized value  $x_{\text{opt}} = 0$  is achieved for the coupling  $J_2/J_1 = 0.40756$ , and we understand this to signal where the Marshall sign rule first fails.

Having established confidence in our numerical implementation, we proceed with unbiased optimization calculations using a static sublattice assignment on lattices up to size  $L = 32$ . Convergence is limited by statistical uncertainty in the (energy to bond count) correlation function that determines the local energy gradient,<sup>33</sup> and it is difficult to reliably optimize for larger system sizes. We first consider the checkerboard AB pattern. At  $g = 0$ , the bond amplitudes are given an initial value of

$$h(x, y) = [\min(x, L - x)^2 + \min(y, L - y)^2]^{-3/2} \quad (14)$$

for  $|x| + |y|$  odd and zero otherwise. The new set of amplitudes obtained from this first run serves as the input for

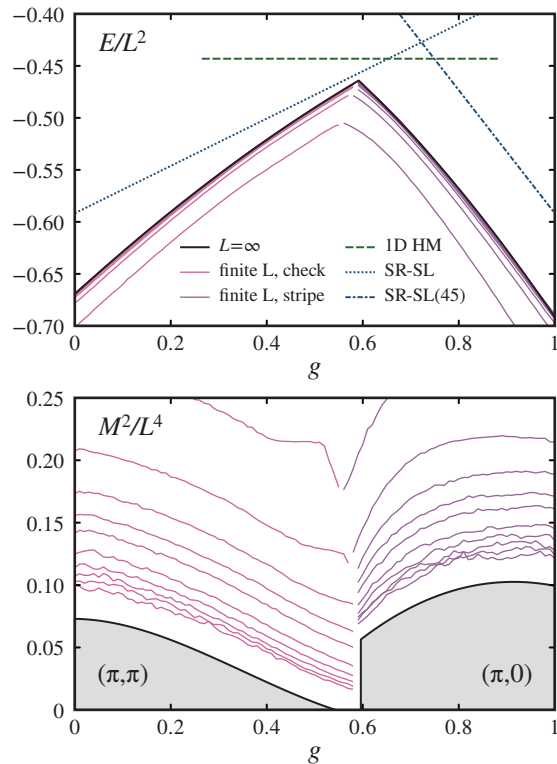


FIG. 6. (color online) (Upper panel) The energy per site versus the coupling ratio. The solid lines are best energies from the trial wavefunction optimization. From bottom to top, system sizes  $L = 4, 6, 8, 10, 12, 16, 20, 24, 28, 32$  are shown. The solid black line, providing an upper envelope to the curves, represents the extrapolation to  $L = \infty$ . The energies of the short range RVB state and of the Heisenberg model on the one-dimensional chain are shown for comparison. (Lower panel) Magnetization data is shown, with the same system sizes now increasing from top to bottom. The solid black lines above the grey shading are the  $L = \infty$  extrapolation. The magnetic order for  $\mathbf{Q} = (\pi, \pi)$  and  $\mathbf{Q} = (\pi, 0)$  both vanish in the small region between  $g_{c1} \doteq 0.54(1)$  and  $g_{c2} \doteq 0.5891(3)$ .

the next optimization process. That is to say, we daisy chain the calculations, at each step using  $g$  to seed the simulation at  $g + \delta g$ . An analogous procedure is carried out for the stripe AB pattern, starting from  $g = \infty$  and stepping the relative coupling down.

One finds that the two sets of simulations do not join smoothly but instead meet with strongly opposite slopes  $\partial \langle H \rangle_{\text{opt}} / \partial g$ . A detailed extrapolation to the thermodynamic limit, presented in Fig. 5, puts the location of the energy level crossing at  $g_{c2} \doteq 0.5891(3)$ . As Fig. 6 makes clear, this point represents the rightmost edge of an intermediate phase that is magnetically disordered. The leftmost edge sits at  $g_{c1} \doteq 0.54(1)$ , where the  $\mathbf{Q} = (\pi, \pi)$  antiferromagnetism vanishes in a continuous fashion.

An important detail is that the optimizations are carried out with the bond amplitudes constrained to have x-

and y-axis reflection symmetry but not  $90^\circ$  rotation symmetry. In the case of the checkerboard simulation, the amplitudes nonetheless realize the full lattice symmetry under optimization up to large values of the relative coupling. For small lattice sizes  $L = 4, 6, 8$ , the symmetry breaks down beyond values  $g \approx 0.51, 0.55, 0.57$ . For all larger sizes, that point is pushed well to the right of  $g_{c2}$ . This means that  $h(\mathbf{r})$  shares a common symmetry across both the staggered magnetic phase and the disordered intermediate phase. But it experiences a sudden break at the onset of stripe magnetic order, dropping from  $C_4$  to  $C_2$ .

In the vicinity of  $g = 0$ , the optimized bond amplitudes are positive definite and an almost perfect function of bond length. As the frustration increases, the amplitudes begin to deviate from circular symmetry, developing strong lobes of weight along the x and y axes. Bonds not aligned along those preferred directions become increasingly short ranged, and the eight knight's move bonds, equivalent to  $h(2, 1)$ , start to trend through zero to negative values. The extrapolation shown in Fig. 7 pinpoints the breakdown of the Marshall sign rule at  $g_{M1} \doteq 0.398(4)$ . What this suggests is that there is strict adherence to a checkerboard Marshall sign rule only below  $g_{M1}$ ; in the range  $g_{M1} < g < g_{c2}$ , the sign rule is violated even though the overall sign structure is still partially consistent with the checkerboard pattern. We find that the behaviour on the large coupling side is not comparable. There, the coupling at which bonds first go

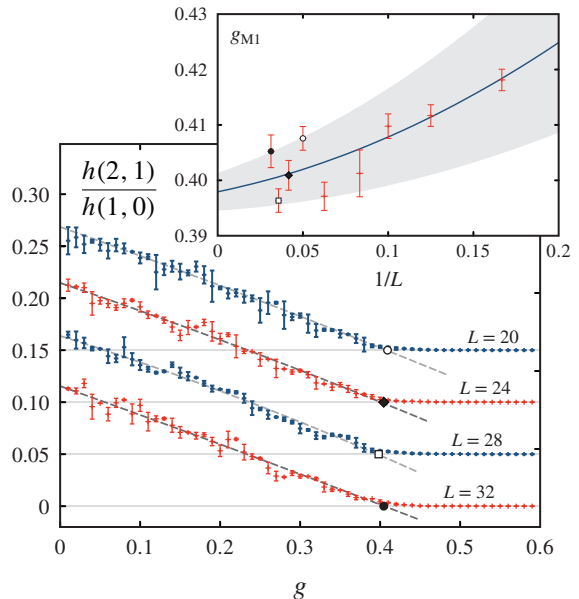


FIG. 7. (color online) The coupling strength at which the amplitude  $h(1, 2)$  extrapolates to zero is plotted against the inverse linear system size. The shaded region represents the envelope containing plausible fits. We estimate that the checkerboard Marshall sign rule fails at  $g_{M1} \doteq 0.398(4)$  in the thermodynamic limit.



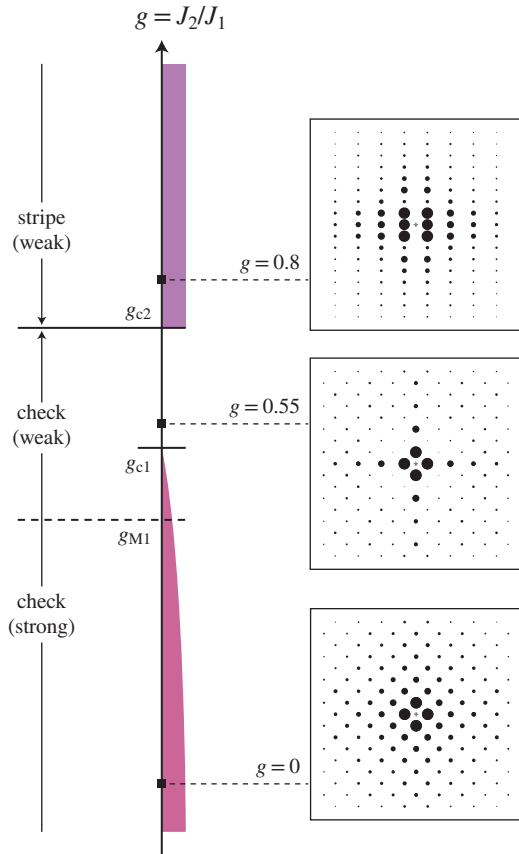


FIG. 8. (color online) Schematic representation of the model's zero temperature phase diagram. Critical couplings  $g_{c1}$  and  $g_{c2}$  mark the boundaries of the magnetically disordered phase. Staggered order ends with a continuous transition at  $g_{c1}$ ; stripe order ends with a first-order transition at  $g_{c2}$ . The three diagrams on the right illustrate the optimized  $h(\mathbf{r})$  values at  $g = 0$ ,  $g = 0.55$ , and  $g = 0.8$ . Each circle, offset by a vector  $\mathbf{r}$  measured from the centre, has an area proportional to the corresponding  $h(\mathbf{r})$  value. The tags on the left indicate the Marshall sign structure that predominates.

negative scales as  $g_{M2} \sim 1/L^4$  and hence does not converge in the thermodynamic limit. We interpret this to mean that the static stripe pattern is only ever a weak description of the Marshall sign structure. See Fig. 8.

We have attempted to confirm this picture by running simulations in which the Marshall sign structure is determined dynamically. More specifically, we want to verify that the strongly first-order transition at  $g_{c2}$  is not merely an artifact of two incompatible sublattice conventions colliding. If permitted, might the system smoothly interpolate over some range of  $g$ , with the peak in  $\Lambda(\mathbf{Q})$  migrating from  $(\pi, \pi)$  to  $(\pi, 0)$ ? We follow the procedure outlined in Sect. IID, whereby the sublattice labelling is no longer fixed and the worm motion itself is allowed to reconfigure the current AB pattern. Our approach is to simulate for various  $g$  values—with *no* daisy chaining—

in each case starting from a random AB pattern and a random loop configuration. The bond amplitudes are initialized with  $h(\mathbf{r})$  forming a broad peak around  $\mathbf{r} = \mathbf{0}$  and having no zero entries. We perform a crude simulation in which any sign associated with the worm moves is thrown away. Otherwise, the optimization of  $h(\mathbf{r})$  proceeds as before. What we find is a result that exactly tracks the state of lower energy produced by assuming one of the two static AB patterns. The simulation flows to the checkerboard for all  $g < g_{c2}$  and to the stripe for all  $g > g_{c2}$ ; the peak in  $\Lambda(\mathbf{Q})$  jumps discontinuously. Obviously we should not read too much into a result that follows from an uncontrolled approximation (sampling by ignoring the signs), but it does give us a sense that the stability of the checkerboard pattern through the intermediate phase and the abrupt change in Marshall sign structure at  $g_{c2}$  might be genuine features of the model.

Given our choice of trial wavefunction, the intermediate phase that we compute is certainly not a bond crystal. The dimer correlations are somewhat enhanced in the strongly frustrated region, but with increasing lattice size they show clear convergence to zero. Still, spatially resolved dimer correlations do give us important information. One can see in Fig. 9 that the optimized state shows the same pattern of dimer correlation and anticorrelation as the short-bond-only RVB but it decays much faster as a function of dimer separation. The comparison is made more explicit in Fig. 10, which shows correlations along a line and a stack of dimers. The functions measured are

$$\begin{aligned} C_{\text{line}}(d) &= \langle \hat{D}(0,0) \hat{D}(d,0) \rangle - \langle \hat{D}(0,0) \rangle \langle \hat{D}(d,0) \rangle \\ C_{\text{stack}}(d) &= \langle \hat{D}(0,0) \hat{D}(0,d) \rangle - \langle \hat{D}(0,0) \rangle \langle \hat{D}(0,d) \rangle, \end{aligned} \quad (15)$$

which we have expressed in terms of the x-directed bond operator  $\hat{D}(x,y) = \mathbf{S}(x,y) \cdot \mathbf{S}(x+1,y)$ .

#### IV. CONCLUSIONS

We have used an optimized valence bond trial wavefunction to study the square-lattice  $J_1$ - $J_2$  Heisenberg model, with an eye to both mapping out the zero-temperature phase diagram and determining how the Marshall sign structure breaks down near the phase boundaries. In the first instance, we fix the AB sublattice labelling to coincide with the order that exists at small and large coupling. For each lattice size, the intermediate phase is approached in two independent simulations (or, rather, chains of history-dependent simulations) by evolving the states progressively out of the two ordered phases, minimizing their energy at each step.

Finite-size scaling of the dimer order parameter suggests that there is no long-range dimer order for any range of  $g$  values. This is to be expected, since the trial state explicitly ignores bond-bond correlations. Measurements of the staggered magnetization show clear evidence of a continuous phase transition in which the staggered

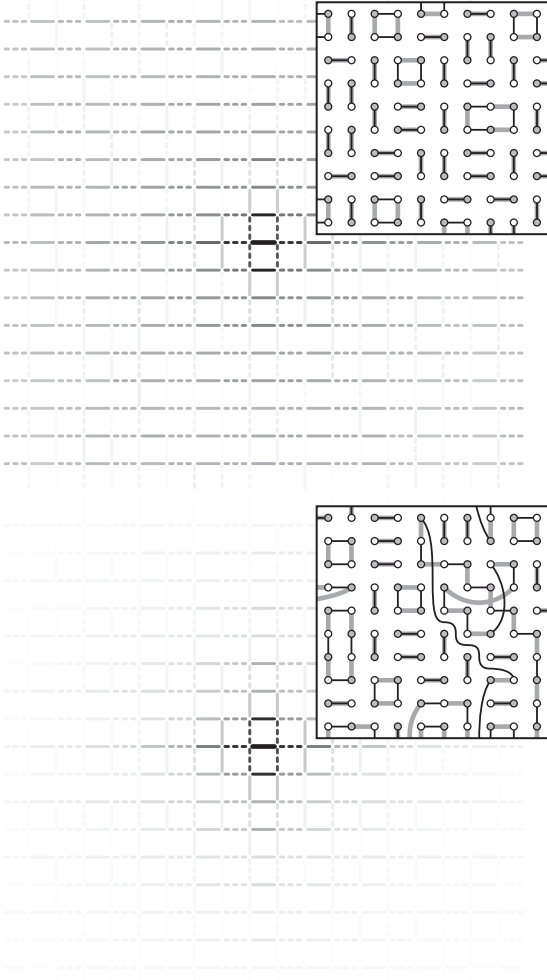


FIG. 9. Grid lines depict the dimer correlations  $C_{ijkl} = \langle (\mathbf{S}_i \cdot \mathbf{S}_j)(\mathbf{S}_k \cdot \mathbf{S}_l) \rangle$  on the nearest-neighbour links  $(k, l)$  of the square lattice, measured with respect to the thick, dark dimer  $(i, j)$  at the centre. The correlations are computed for the  $L = 28$  system. The grayscale intensity represents correlation strength [presented as the fourth power of  $(1 + 1.5r^{1.5})C$ ], and dotted lines indicate a negative (anticorrelated) value. The top panel shows results for the purely short ranged RVB state, presented for comparison's sake. The bottom panel shows results for the energy-optimized state at  $g = 0.58$ . In each case, a  $10 \times 10$  piece of the of the full valence bond loop configuration, obtained from a snapshot of the Monte Carlo simulation, is overlaid.

magnetization vanishes at  $g_{c1} \doteq 0.54(1)$ . On the other edge of the intermediate phase, an energy level crossing at  $g_{c2} \doteq 0.5891(3)$  results in the sudden disappearance of the otherwise robust stripe magnetization. This is accompanied by the restoration of the system's rota-

tional symmetry. (Since the trial state is least able to describe the intermediate phase—again, because of its lack of bond-bond correlations—we should probably view  $g_{c1}$  and  $g_{c2}$  as upper and lower bounds, respectively, on the true positions of the phase boundaries.) We have also performed calculations in which no sublattice labelling is put in by hand. Our results suggest that the checkerboard AB pattern is the correct choice throughout the intermediate phase. Hence, within the context our trial wavefunction scheme, we surmise that the state beyond  $g_{c1}$  is a “bosonic” gapped spin liquid, and the gap to its excitations has a minimum at  $(\pi, \pi)$ .

Figure 8 gives a quick summary of our results. We observe that at high frustration the bond amplitudes take on a highly anisotropic form. This is quite different from the long-bond to short-bond picture that is usually invoked. Recall that Liang, Ducot, and Anderson studied long range RVB states on the square lattice with amplitudes  $h \sim r^{-p}$  that decay as a powerlaw in the bond length  $r$ .<sup>28</sup> In that framework, the state becomes magnetically disordered when  $p$  exceeds a critical value of 3.3,<sup>30,85,86</sup> and the entire family of states in the range  $p > 3.3$  is continuously connected to  $p = \infty$ , which is the short-bond-only RVB. The intermediate phase state obtained in our simulations is of a quite different character. The state is magnetically disordered not because its bond amplitudes are sufficiently short ranged but because they are sufficiently anisotropic.

This work was supported by a Discovery grant from NSERC of Canada.

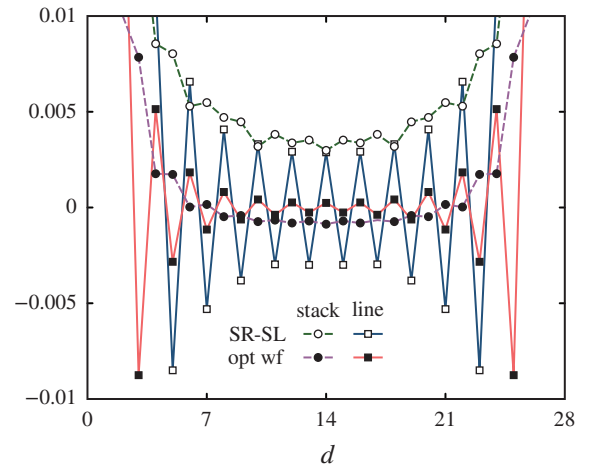


FIG. 10. (color online) Dimer correlations of the product-amplitude trial wavefunction optimized at  $g = 0.58$  (solid points) and the short-bond-only RVB state (open points) are compared on the  $L = 28$  lattice. Presented are the dimer line (squares) and dimer stack (circles) correlation functions. See the text for definitions.

\* Electronic mail: kbeach@ualberta.ca

<sup>1</sup> A. H. MacDonald, S. M. Girvin, and D. Yoshioka, Phys.

- Rev. B **37**, 9753 (1988); A. H. MacDonald, S. M. Girvin, and D. Yoshioka, Phys. Rev. B **41**, 2565 (1990).
- <sup>2</sup> S. Fujimoto, Phys. Rev. B **72**, 024429 (2005).
  - <sup>3</sup> A. Läuchli, J. C. Domenge, C. Lhuillier, P. Sindzingre, and M. Troyer, Phys. Rev. Lett. **95**, 137206 (2005).
  - <sup>4</sup> A. W. Sandvik, Phys. Rev. Lett. **98**, 227202 (2007).
  - <sup>5</sup> K. S. D. Beach and A. W. Sandvik, Phys. Rev. Lett. **99**, 047202 (2007).
  - <sup>6</sup> K. Majumdar, D. Furton, and G. S. Uhrig, Phys. Rev. B **85**, 144420 (2012).
  - <sup>7</sup> "Frustrated spin systems," H. T. Diep editor, World-Scientific (2005). ISBN 981-256-091-2
  - <sup>8</sup> "Introduction to Frustrated Magnetism: Materials, Experiments, Theory," Springer (2011). ISBN 978-364-210-588-3
  - <sup>9</sup> P. W. Anderson, Mater. Res. Bull. **8**, 153 (1973).
  - <sup>10</sup> I. Affleck and J. B. Marston, Phys. Rev. B **37**, 374 (1988).
  - <sup>11</sup> N. Read and S. Sachdev, Phys. Rev. Lett. **62**, 1694 (1989)
  - <sup>12</sup> G. Misguich, C. Lhuillier, M. Mambrini, and P. Sindzingre, Eur. Phys. J. B **26**, 167 (2002).
  - <sup>13</sup> M. B. Hastings, Phys. Rev. B **69**, 104431 (2004).
  - <sup>14</sup> W. Marshall, Proc. Roy. Soc. A **48**, 232 (1955).
  - <sup>15</sup> B. B. Beard, U.-J. Wiese, Phys. Rev. Lett. **77**, 5130 (1996).
  - <sup>16</sup> O. F. Syljuåsen and A. W. Sandvik, Phys. Rev. E **66**, 046701 (2002).
  - <sup>17</sup> H. G. Evertz, Adv. Phys. **52**, 1 (2003).
  - <sup>18</sup> G. Rumer, Gottingen Nachr. Tech. **1932**, 377 (1932).
  - <sup>19</sup> L. Pauling, J. Chem. Phys. **1**, 280 (1933)
  - <sup>20</sup> L. Hulthén, Ark. Mat. Atron. Fys. **26a**, 1 (1938).
  - <sup>21</sup> P. Fazekas and P. W. Anderson, Philos. Mag. **30**, 23 (1974).
  - <sup>22</sup> K. S. D. Beach and A. W. Sandvik, Nucl. Phys. B **750**, 142 (2006).
  - <sup>23</sup> K. S. D. Beach, M. Mambrini, and F. Alet, Phys. Rev. B **77**, 146401 (2008).
  - <sup>24</sup> S. Liang, Phys. Rev. B **42**, 65555 (1990); Phys. Rev. Lett. **64**, 1597 (1990).
  - <sup>25</sup> G. Santoro, S. Sorella, L. Guidoni, A. Parola, and E. Tosatti, Phys. Rev. Lett. **83**, 3065 (1999).
  - <sup>26</sup> A. W. Sandvik, Phys. Rev. Lett. **95**, 207203 (2005).
  - <sup>27</sup> A. W. Sandvik and H. G. Evertz, Phys. Rev. B **82**, 024407 (2010).
  - <sup>28</sup> S. Liang, B. Doucot, and P. W. Anderson, Phys. Rev. Lett. **95**, 207203 (2005).
  - <sup>29</sup> Y.-C. Lin, Y. Tang, Jie Lou, A. W. Sandvik, arXiv:1206.6803v2.
  - <sup>30</sup> K. S. D. Beach, arXiv:0707.0297.
  - <sup>31</sup> In the more familiar spin-wave language, the justification is the weak interaction between magnons at long range; see N. Hasselmann and P. Kopietz, Europhys. Lett. **74**, 1067 (2006).
  - <sup>32</sup> P. Chandra, P. Coleman, and A. I. Larkin, Phys. Rev. Lett. **64**, 88 (1990).
  - <sup>33</sup> J. Lou and A. W. Sandvik, Phys. Rev. B **76**, 104432 (2007).
  - <sup>34</sup> K. S. D. Beach, Phys. Rev. B **79**, 224431 (2009).
  - <sup>35</sup> A. F. Albuquerque and F. Alet, Phys. Rev. B **82**, 180408(R) (2010).
  - <sup>36</sup> Y. Tang, A. W. Sandvik, C. L. Henley, Phys. Rev. B **84**, 174427 (2011).
  - <sup>37</sup> E. Dagotto and A. Moreo, Phys. Rev. Lett. **63**, 2148 (1989).
  - <sup>38</sup> H. J. Schulz, T. A. L. Ziman, and D. Poilblanc, J. Phys. I France, **6**, 675 (1996).
  - <sup>39</sup> J. Oitmaa and Z. Weihong, Phys. Rev. B **54**, 3022 (1996).
  - <sup>40</sup> R. F. Bishop, D. J. J. Farnell and J. B. Parkinson, Phys. Rev. B **58**, 6394 (1998).
  - <sup>41</sup> R. R. P. Singh, Z. Weihong, C. J. Hamer, and J. Oitmaa, Phys. Rev. B **60**, 7278 (1999).
  - <sup>42</sup> O. P. Sushkov, J. Oitmaa, and W. Zheng, Phys. Rev. B **63**, 104420 (2001).
  - <sup>43</sup> E. Y. Loh Jr., J. E. Gubernatis, R. T. Scalettar, S. R. White, D. J. Scalapino, and R. L. Sugar, Phys. Rev. B **41**, 9301 (1990).
  - <sup>44</sup> J. Richter, J. Schulenburg, A. Honecker, and D. Schmalzfuß, Phys. Rev. B **70**, 174454 (2004).
  - <sup>45</sup> J. Richter, J. Schulenburg, Eur. Phys. J. B **73**, 117 (2010).
  - <sup>46</sup> A. M. Läuchli, J. Sudan, E. S. Sørensen, Phys. Rev. B **83**, 212401 (2011).
  - <sup>47</sup> A. M. Läuchli and R. Johanni, APS March Meeting **57**, 1 (2012). [<http://meetings.aps.org/link/BAPS.2012.MAR.H8.7>]
  - <sup>48</sup> P. W. Anderson, Science **235** 1196 (1987).
  - <sup>49</sup> L. Capriotti, F. Becca, A. Parola, and S. Sorella, Phys. Rev. Lett. **87**, 097201 (2001).
  - <sup>50</sup> S. Yunoki and S. Sorella, Phys. Rev. Lett. **92**, 157003 (2004).
  - <sup>51</sup> J. Cano and P. Fendley, Phys. Rev. Lett. **105**, 067205 (2010).
  - <sup>52</sup> T. Li, F. Becca, W. Hu, S. Sorella, arXiv:1205.3838v1.
  - <sup>53</sup> A. Moreo, E. Dagotto, Th. Jolicoeur, and J. Riera, Phys. Rev. B **42**, 6283 (1990).
  - <sup>54</sup> A. Chubukov, Phys. Rev. B **44**, 392 (1991).
  - <sup>55</sup> J. Ferrer, Phys. Rev. B **47**, 8769 (1993).
  - <sup>56</sup> H. A. Ceccatto, C. J. Gazza, and A. E. Trumper, Phys. Rev. B **47**, 12329 (1993).
  - <sup>57</sup> M. P. Gelfand, R. R. P. Singh, and D. A. Huse, Phys. Rev. B **40**, 10801 (1989).
  - <sup>58</sup> M. P. Gelfand, Phys. Rev. B **42**, 8206 (1990).
  - <sup>59</sup> R. R. P. Singh and R. Narayanan, Phys. Rev. Lett. **65**, 1072 (1990)
  - <sup>60</sup> M. E. Zhitomirsky and K. Ueda, Phys. Rev. B **54**, 9007 (1996).
  - <sup>61</sup> P. W. Leung and N. W. Lam, Phys. Rev. B **53**, 2213 (1996).
  - <sup>62</sup> V. N. Kotov, J. Oitmaa, O. P. Sushkov, and Z. Weihong, Phys. Rev. B **60**, 14613 (1999) [CAS].
  - <sup>63</sup> V. N. Kotov and O. P. Sushkov, Phys. Rev. B **61**, 11820 (2000) [CAS].
  - <sup>64</sup> L. Capriotti and S. Sorella, Phys. Rev. Lett. **84**, 3173 (2000).
  - <sup>65</sup> K. Takano, Y. Kito, Y. ?no, and K. Sano, Phys. Rev. Lett. **91**, 197202 (2003).
  - <sup>66</sup> M. Mambrini, A. Läuchli, D. Poilblanc, and F. Mila, Phys. Rev. B **74**, 144422 (2006).
  - <sup>67</sup> V. Murg, F. Verstraete, and J. I. Cirac, Phys. Rev. B **79**, 195119 (2009).
  - <sup>68</sup> J. Reuther and P. Wölfe, Phys. Rev. B **81**, 144410 (2010).
  - <sup>69</sup> J. Reuther, P. Wölfe, R. Darradi, W. Brenig, M. Arlego, and J. Richter, Phys. Rev. B **83**, 064416 (2011).
  - <sup>70</sup> J.-F. Yu and Y.-J. Kao, Phys. Rev. B **85**, 094407 (2012).
  - <sup>71</sup> P. Chandra and B. Doucot, Phys. Rev. B **38**, 9335 (1988).
  - <sup>72</sup> F. Figureirido, A. Karlhede, S. Kivelson, S. Sondhi, M. Rocek, and D. S. Rokhsar, Phys. Rev. B **41**, 4619 (1990).
  - <sup>73</sup> T. Oguchi and H. Kitatani, J. Phys. Soc. Jpn. **59**, 3322 (1990).
  - <sup>74</sup> P. Locher, Phys. Rev. B **41**, 2537 (1990).
  - <sup>75</sup> H. J. Schulz and T. A. L. Ziman, Europhys. Lett. **18**, 355 (1992).
  - <sup>76</sup> Q. F. Zhong and S. Sorella, Europhys. Lett. **21**, 629 (1993).

- <sup>77</sup> G.-M. Zhang, H. Hu, and L. Yu, Phys. Rev. Lett. **91**, 067201 (2003).
- <sup>78</sup> L. Capriotti, F. Becca, A. Parola, and S. Sorella, Phys. Rev. B **67**, 212402 (2003).
- <sup>79</sup> L. Capriotti, D. J. Scalapino, and S. R. White, Phys. Rev. Lett. **93**, 177004 (2004).
- <sup>80</sup> L. Capriotti and S. Sachdev, Phys. Rev. Lett. **93**, 257206 (2004).
- <sup>81</sup> L. Wang, Z. C. Gu, X. G. Wen, and F. Verstraete, arXiv:1112.3331v2.
- <sup>82</sup> H.-C. Jiang, H. Yao, and L. Balents, arXiv:1112.2241v1.
- <sup>83</sup> A. W. Sandvik, Phys. Rev. B **85** 134407 (2012).
- <sup>84</sup> N. Prokof'ev and B. Svistunov, Phys. Rev. Lett. **87**, 160601 (2001).
- <sup>85</sup> M. Havig and A. Auerbach, Phys. Rev. Lett. **83**, 4848 (1999).
- <sup>86</sup> M. Havig and A. Auerbach, Phys. Rev. B **62**, 324 (2000).
- <sup>87</sup> D. H. Lehmer, Proc. Sympos. Appl. Math. Combinatorial Analysis, Amer. Math. Soc. **10**, 179 (1960).
- <sup>88</sup> D. E. Knuth, "Volume 3: Sorting and Searching," The Art of Computer Programming, Addison-Wesley, pp. 12, (1973). ISBN 0-201-89685-0
- <sup>89</sup> M. S. Block, R. K. Kaul, arXiv:1205.3530v1.
- <sup>90</sup> R. K. Kaul, R. G. Melko, A. W. Sandvik, arXiv:1204.5405v1.
- <sup>91</sup> A. W. Sandvik and R. Moessner, Phys. Rev. B **73**, 144054 (2006).

n	$C_1$	$C_2$	$Z$	$M^2(\pi, \pi)$	$M^2(\pi, 0)$	$D$
0	22241280	9902080	1559232	113983488	17383424	4376064
1	194568192	104726528	13008384	1117618176	139902976	28540928
2	997232640	585695232	66018816	6104383488	709410816	127591424
3	3395051520	2137292800	223842816	21861335040	2381496320	389861376
4	8564477952	5689352192	568694016	57653526528	6069354496	932687872
5	16547069952	11594661888	1108661760	116342292480	11792498688	1697314816
6	25797685248	18932629504	1767412224	189239033856	18888998912	2580870144
7	32679444480	25148850176	2302253568	250229981184	24519589888	3165620224
8	34418749440	27661209600	2528419968	275349995520	27030159360	3329164288
9	29878050816	25148850176	2302253568	250229981184	24519589888	2857185280
10	21512073216	18932629504	1767412224	189239033856	18888998912	2089987072
11	12538503168	11594661888	1108661760	116342292480	11792498688	1223688192
12	5848903680	5689352192	568694016	57653526528	6069354496	594391040
13	2070282240	2137292800	223842816	21861335040	2381496320	218601472
14	528863232	585695232	66018816	6104383488	709410816	60980224
15	84836352	104726528	13008384	1117618176	139902976	11331584
16	6254592	9902080	1559232	113983488	17383424	1074688

TABLE I. The integer coefficients for the rational polynomial that expresses various measured quantities for the product amplitude trial state on the  $4 \times 4$  lattice. The columns correspond to the nearest- and next-nearest-neighbour spin correlations, the partition function (denominator), the staggered and stripe magnetization, and the columnar dimer order parameter.